

Dissipative structures in a parametrically driven dissipative lattice: Chimera, localized disorder, continuous-wave, and staggered states

A.M. Cabanas^{a,*}, J.A. Vélez^b, L.M. Pérez^b, P. Díaz^c, M.G. Clerc^d, D. Laroze^{b,**}, B.A. Malomed^e

^a Sede Esmeralda, Universidad de Tarapacá, Av. Luis Emilio Recabarren Iquique, 2477, Chile

^b Instituto de Alta Investigación, CEDENNA, Universidad de Tarapacá, Casilla 7D, Arica, Chile

^c Departamento de Ciencias Físicas, Universidad de La Frontera, Casilla 54-D, Temuco, Chile

^d Departamento de Física and Millennium Institute for Research in Optics, Facultad de Ciencias Físicas y Matemáticas, Universidad de Chile, Casilla Santiago, 4873, Chile

^e Department of Physical Electronics, School of Electrical Engineering, Faculty of Engineering, and Center for Light-Matter Interaction, Tel Aviv University, Tel Aviv IL-69978, Israel

ARTICLE INFO

Article history:

Received 19 February 2021

Accepted 13 March 2021

Keywords:

Chaos

Chimera states

Localized disorder

ABSTRACT

Discrete dissipative coupled systems exhibit complex behavior such as chaos, spatiotemporal intermittence, chimeras among others. We construct and investigate chimera states, in the form of confined stationary and dynamical states in a chain of parametrically driven sites with onsite damping and cubic nonlinearity. The system is modeled by the respective discrete parametrically driven damped nonlinear Schrödinger equation. Chimeras feature quasi-periodic or chaotic dynamics in the filled area, quantified by time dependence of the total norm (along with its power spectrum), and by the largest Lyapunov exponent. Systematic numerical simulations, in combination with some analytical results, reveal regions in the parameter space populated by stable localized states of different types. A phase transition from the stationary disordered states to spatially confined dynamical chaotic one is identified. Essential parameters of the system are the strength and detuning of the forcing, as well as the lattice's coupling constant.

© 2021 Elsevier Ltd. All rights reserved.

1. Introduction

Coupled oscillators are of great interest owing to their wide applicability in physics, chemistry, and biology (see Refs. [1–6] and references therein). Likewise, these systems attract global attention due to their dynamic behavior, such as synchronization, defects and/or phase turbulence, defect-mediated turbulence, spatiotemporal intermittency, and coexisting coherent and incoherent states, among others [1,6,7]. In the last few decades, a great deal of effort has been devoted to understand the coexistence of coherent and incoherent domains called chimera states. These states were introduced by Kuramoto and Battogtokh [8]. This finding came as a surprise because the oscillators were identical and symmetrically coupled. Nevertheless, along with regular synchronized dynamics, the coupled oscillator lattices exhibit incoherent or desynchronized behavior. The understanding of the symmetry breaking, which leads to the emergence of chimeras in dissipative systems [9], is a significant issue as it appears in different contexts, such

as biological models, delayed systems, metamaterials, coupled map lattices, quantum systems, networks, and even in a population of social agents, to mention a few [10–30].

As concerns dynamical elements of which lattices may be built, a paradigmatic example of forced nonlinear oscillators is provided by the parametrically driven damped nonlinear Schrödinger equation [31]. It models resonant phenomena in nonlinear dispersive media and gives rise to soliton solutions with a variety of dynamical behavior [32–35], Faraday waves [36], breathers [37,38], two-soliton states [39,40] and other soliton complexes [41], and spatiotemporal chaos [42]. Generalizations of this equation and its applications can be found in Refs. [41,43–57].

In many physical realizations, this equation is replaced by its lattice counterpart, in the framework of the class of models known as discrete nonlinear Schrödinger (DNLS) equations [58,59]. These equations furnish fundamental models in discrete nonlinear optics [60–68], as well as for Bose–Einstein condensates trapped and fragmented in deep optical-lattice potentials [69–72]. In particular, the stability of discrete solitons in the parametrically driven DNLS equations, both conservative and dissipative ones, has been studied in Refs. [73–78].

The present work aims to study and build up chimera states in arrays of dissipative parametrically driven coupled oscillators

* Corresponding author.

** Co-corresponding author.

E-mail addresses: ana.cabanas.plana@gmail.com (A.M. Cabanas), dlaroz@uta.cl (D. Laroze).

which are described by the damped DNLS equation with the parametric gain applied at its sites. These states appear as patched-shaped (self-confined) patterns filled by waves with a “leaping” spatial structure (see an exact definition below), which are linked by steep transient layers to the stable zero state. When the parameters are modified the chimera states are replaced by a spatially disordered localized one. Such states exist in a stationary form due to the bistability and discrete nature of the system. In particular, we explore the existence of the chimera state as a function of the driving force and its detuning, producing a complete chart for stable stationary and dynamical states in the respective parameter space. All these dynamic behaviors correspond to permanent states of the system out of equilibrium, which correspond to *dissipative structures* in the terminology introduced by Prigogine [79]. Effects of variation of the intersite-coupling strength in the underlying DNLS equation are examined too. We find chaotic chimeras, in addition to regular dynamical states, and the system gives rise to multistability.

The manuscript is organized as follows. The model and some analytical findings for it are presented in Section 2. Results from systematic numerical investigation of the stationary and dynamical states are summarized in Section 3. Conclusions are presented in Section 4.

2. The model and analytical results

2.1. The parametrically driven damped DNLS equation

Let us consider a one-dimensional array of coupled nonlinear oscillators under the action of dissipation and parametric drive. The respective DNLS equation is (cf. Ref. [76])

$$\begin{aligned} \frac{dA^j}{dt} &= -i\epsilon(A^{j+1} + A^{j-1} - 2A^j) \\ &+ \gamma(A^j)^* - i\nu A^j - \alpha A^j - i|A^j|^2 A^j, \end{aligned} \quad (1)$$

where A^j is a complex-valued amplitude at site j , the asterisk symbol stands for the complex conjugation, and t is normalized time. If Eq. (1) models an array of parametrically amplified lossy optical waveguides with the Kerr nonlinearity [80] t , is actually, the propagation distance along each waveguide. Further, $\epsilon > 0$ represents the coupling between adjacent sites in the array, $\gamma > 0$ is the strength of the parametric drive (the sign of $\gamma < 0$ may be inverted by redefining $\tilde{A}^j \equiv iA^j$), ν is the detuning of the drive, and $\alpha > 0$ is the damping constant, while the on-site nonlinearity coefficient is scaled to be 1. Note that the sign of the nonlinear term in Eq. (1) corresponds to the self-focusing onsite nonlinearity; if its original sign is opposite, it may be inverted by means of the staggering transformation [81], that is, $A^j \equiv (-1)^j \exp(-2i\epsilon t)(\tilde{A}^j)^*$. The remaining scaling invariance of Eq. (1) allows us to fix one of the parameters. We use this option to choose the value of the damping coefficient, $\alpha = 0.35$, which is convenient for the presentation of numerical results. The analysis is reported below for negative detuning, $\nu < 0$, which implies a possibility of the existence of the dissipative bright discrete solitons, supported by the self-focusing nonlinearity.

It is relevant to mention that, in addition to the direct realizations of Eq. (1) as the chain of coupled oscillators with the complex amplitudes, the same model can be derived as an asymptotic approximation for a parametrically driven discrete nonlinear Klein-Gordon equation or Frenkel-Kontorava model, i.e., a chain of nonlinear oscillators with real dynamical variables [78]. Fig. 1 illustrates some examples of different physical systems that are described by parametrically driven damped discrete nonlinear Schrödinger Eq. (1). Panel (a) represents a one-dimensional array of forcing coupled-waveguide resonators [12], frame (b) illustrates

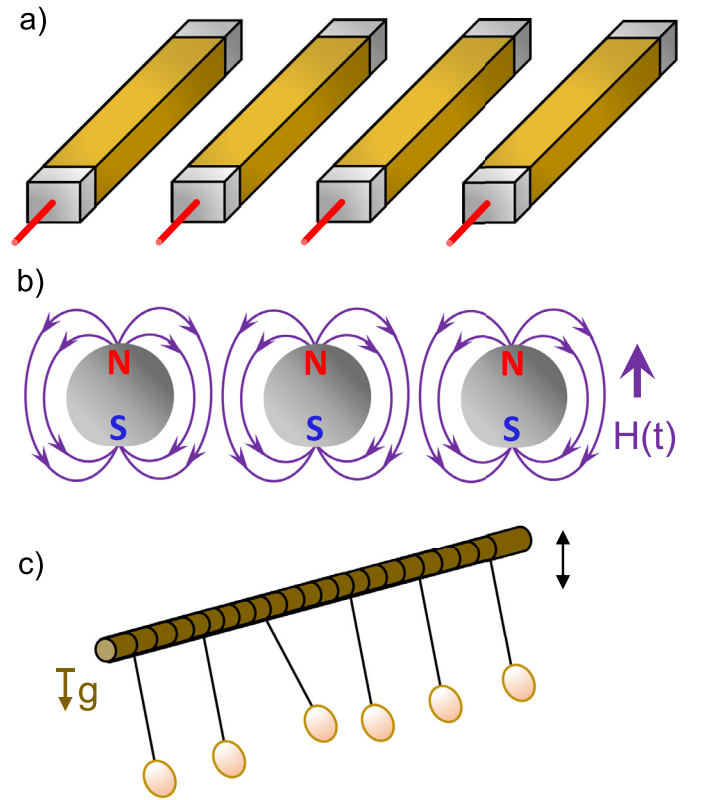


Fig. 1. Parametrically driven damped discrete systems. Schematic representation of a one-dimensional array of forced coupled-waveguide resonators (a), coupled magnets under a time dependent magnetic field (b), and vertically driven coupled pendulums (c).

a set of parametrically driven coupled magnets [38,39,52], while panel (c) depicts a vertically driven coupled pendulums [44].

Stationary solutions to Eq. (1) can be looked for with a constant value of the phase at all sites:

$$A^j = B^j \exp(\mp i\delta_0), \quad \delta_0 \equiv \tan^{-1}\left(\sqrt{\frac{\gamma - \alpha}{\gamma + \alpha}}\right), \quad (2)$$

where real amplitudes B^j obey the stationary version of the usual DNLS equation,

$$\begin{aligned} \epsilon(B^{j+1} + B^{j-1} - 2B^j) + (B^j)^3 = \\ (-\nu \pm \sqrt{\gamma^2 - \alpha^2})B^j. \end{aligned} \quad (3)$$

The top and bottom signs in Eq. (3) correspond to those in Eq. (2).

In simulations reported in this work, we fixed the number of sites in the lattice as $N = 256$, so the discrete coordinate takes values $j = 1, \dots, 256$. We used Neumann boundary conditions at edges of the lattice, which means formally setting $A^0 \equiv A^1$ and $A^{N+1} \equiv A^N$ in Eq. (1) at $j = 1$ and $j = 256$, respectively.

2.2. Stability of the zero state

Because states considered in this work include zero-field segments, such states are relevant solutions if $A^j = 0$ is a stable solution of model Eq. (1). To address the stability of zero, perturbed solutions to the linearized version of Eq. (1) are looked for as a combination of terms $\exp(\Gamma t)\{\cos(kj), \sin(kj)\}$ to derive a dispersion relation for the instability growth rate, Γ , as a function of the perturbation wavenumber k

$$\Gamma = -\alpha \pm \sqrt{\gamma^2 - [4\epsilon \sin^2(k/2) - \nu]^2} \quad (4)$$

(cf. Ref. [82]). It follows from Eq. (4) that stability conditions for the zero state, $\text{Re}(\Gamma(k)) \leq 0$, which must hold for all real values of k , amount to

$$\begin{aligned} \gamma^2 &\leq \alpha^2 + \nu^2 \equiv \gamma_{\max}^2, & \text{at } \nu < 0, \\ \gamma &\leq \alpha, & \text{at } 0 < \nu < 4\epsilon, \\ \gamma^2 &\leq \alpha^2 + (\nu - 4\epsilon)^2, & \text{at } \nu > 4\epsilon. \end{aligned} \quad (5)$$

In the continuum limit, which corresponds to $\epsilon \rightarrow \infty$, or, effectively, to replacement

$$4\epsilon \sin^2(k/2) \rightarrow \epsilon k^2, \quad (6)$$

in Eq. (4), the bottom line in Eq. (5) is irrelevant, while the top and middle ones remain valid, cf. Ref. [36]. In the case of $\gamma^2 > \gamma_{\max}^2$ at $\nu < 0$ [see the top line in Eq. (5)], the instability of the zero state leads to establishment of solutions to Eq. (1) in the form of Faraday patterns, as [36].

2.3. Continuous-wave states: existence conditions

Next, Eq. (3) gives rise to two uniform (“continuous-wave”, CW) solutions with a constant amplitude:

$$B = \sqrt{-\nu \pm \sqrt{\gamma^2 - \alpha^2}} \equiv B_0^{(\pm)}. \quad (7)$$

Eq. (7) also describes the amplitude of lattice solitons, with one or several excited sites, in the *anti-continuum limit*, $\epsilon \rightarrow 0$ [83].

In the case of positive detuning, $\nu > 0$, solution (7) exists only with the top sign, under condition $\gamma^2 > \alpha^2 + \nu^2$, which is incompatible with the middle and bottom lines in Eq. (5), hence in this case, the CW solution cannot coexist with the stable zero state. However, in the case of $\nu < 0$, CW solutions with both signs in Eq. (7) exist in the interval of values of the drive’s strength

$$\alpha^2 < \gamma^2 \leq \alpha^2 + \nu^2, \quad (8)$$

in which the stability condition of the zero solution, given by the top line in Eq. (5), holds. Therefore, in this interval, both the zero state and the CW solution with a larger amplitude, corresponding to the top sign in Eq. (7), may be stable. Note that, according to general principles of the bifurcation theory [86], the latter solution is definitely stable in the anti-continuum limit, with $\epsilon = 0$ in Eq. (1), while the full stability analysis at $\epsilon > 0$ makes it necessary to consider the possibility of the modulational instability, see the following subsection. On the other hand, the intermediate solution, corresponding to the bottom sign in Eq. (7), is definitely unstable, playing the role of a *separatrix* between attraction basins of the two presumably stable states.

With the increase of γ , both CW states, given by Eq. (7), emerge through the *saddle-node bifurcation* [86] at $\gamma = \alpha$. With the subsequent increase of γ , the unstable solution with the smaller amplitude collides with the zero state, and thus disappears, through the *inverse pitchfork bifurcation* [86], at $\gamma^2 = \alpha^2 + \nu^2$ (formally, the latter bifurcation involves solution $B_0^{(-)}$, given by Eq. (7), and its counterpart $-B_0^{(-)}$). The same bifurcation destabilizes the zero solution, as seen from the top line in Eq. (5). At $\gamma^2 > \alpha^2 + \nu^2$, only the CW solution with the top sign in Eq. (7) exists, remaining possibly stable, while the zero state is unstable.

Thus, stable zero and CW states coexist in interval (8), under the condition of $\nu < 0$. Nevertheless, it is impossible to build up a transient layer or domain wall (front solution) connecting these states, with exponentially decaying tails approaching each one. Indeed, the tail approaching the zero state can be looked for as the following solution to the linearized version of Eq. (3)

$$B^j = b_0 \exp(-q|j|), \quad (9)$$

at $|j| \rightarrow \infty$, with some constant b_0 and the spatial decay rate, q , determined by expression

$$\sinh^2(q/2) = (4\epsilon)^{-1} \left(-\nu \pm \sqrt{\gamma^2 - \alpha^2} \right), \quad (10)$$

where the top and bottom signs correspond to those in Eqs. (7) and (9). On the other hand, the tail approaching the CW state is looked for as

$$B^j = B_0^{(\pm)} + \tilde{b}_0 \exp(-p|j|), \quad (11)$$

with another constant \tilde{b}_0 and the decay rate p determined by Eq. (3) linearized around $B = B_0^{(\pm)}$:

$$\sinh^2(p/2) = -(2\epsilon)^{-1} \left(-\nu \pm \sqrt{\gamma^2 - \alpha^2} \right). \quad (12)$$

Obviously, conditions $\sinh^2(q/2) > 0$ and $\sinh^2(p/2) > 0$, which are necessary for the existence of the transient layer, are incompatible, as it follows from Eqs. (10) and (12). Therefore, localized patterns in the form of finite-width patches of CW connected by smooth fronts to the stable zero state do not exist. Nevertheless, we find that, at $\epsilon < 0.44$, flat localized states filled by the CW do exist, being bounded by layers which include sharp edge peaks, hence they cannot be approximated by ansatz (11) [87,88].

Localized states produced by Eq. (1) are the main subject of this work. These states are built as localized patches filled not by flat CW states, but rather by ones spatially oscillating between different amplitude levels (*leaping waves*, LWs). Chimera states are built as spatiotemporal incoherent segments set on top of the stable zero background. Example of them are shown in Figs. 2(c), 3(a) and 4 below and explained in detail in Section 2.5.

In this framework, it is worth to mention that solutions for smooth transient layers connecting zero and CW states, in spite of being impossible in the present system, are admitted by models including competing nonlinearities. Known examples are provided by equations including cubic-quintic [89] or quadratic-cubic [90] combinations of self-focusing and defocusing terms.

2.4. Modulational stability of the CW state

It is also relevant to address the modulational (in)stability of the CW state given by expressions (2) and (7). As it is well known, the constant-amplitude solution of the usual DNLS equation with the self-focusing sign of the onsite nonlinearity is always unstable, in the absence of the damping and parametric drive [84]. In the present case, a perturbed form of the CW solution is sought for as

$$A^j(t) = B_0^{(\pm)} [1 + a_j(t)] \exp[\mp i\delta_0 + i\chi_j(t)], \quad (13)$$

where \mp has the same meaning as in Eq. (2). The substitution of this expression in Eq. (1) and the subsequent linearization with respect to small perturbations, $a_j(t)$ and $\chi_j(t)$, leads to a system with the following evolution equations for the perturbations,

$$\begin{aligned} \frac{da_j}{dt} &= \epsilon(\chi_{j+1} + \chi_{j-1} - 2\chi_j) \\ &\quad - 2\gamma \sin(2\delta)\chi_j, \\ \frac{d\chi_j}{dt} &= -\epsilon(a_{j+1} + a_{j-1} - 2a_j) \\ &\quad - 2(B_0^{(\pm)})^2 a_j - 2\gamma \cos(2\delta)\chi_j. \end{aligned} \quad (14)$$

Eigenmodes of the small perturbations, with instability growth rate σ (that may be complex-valued) and real wavenumber k , are looked for in the usual form,

$$\{a_j(t), \chi_j(t)\} = \{a^{(0)}, \chi^{(0)}\} \exp(ikj + \sigma t). \quad (15)$$

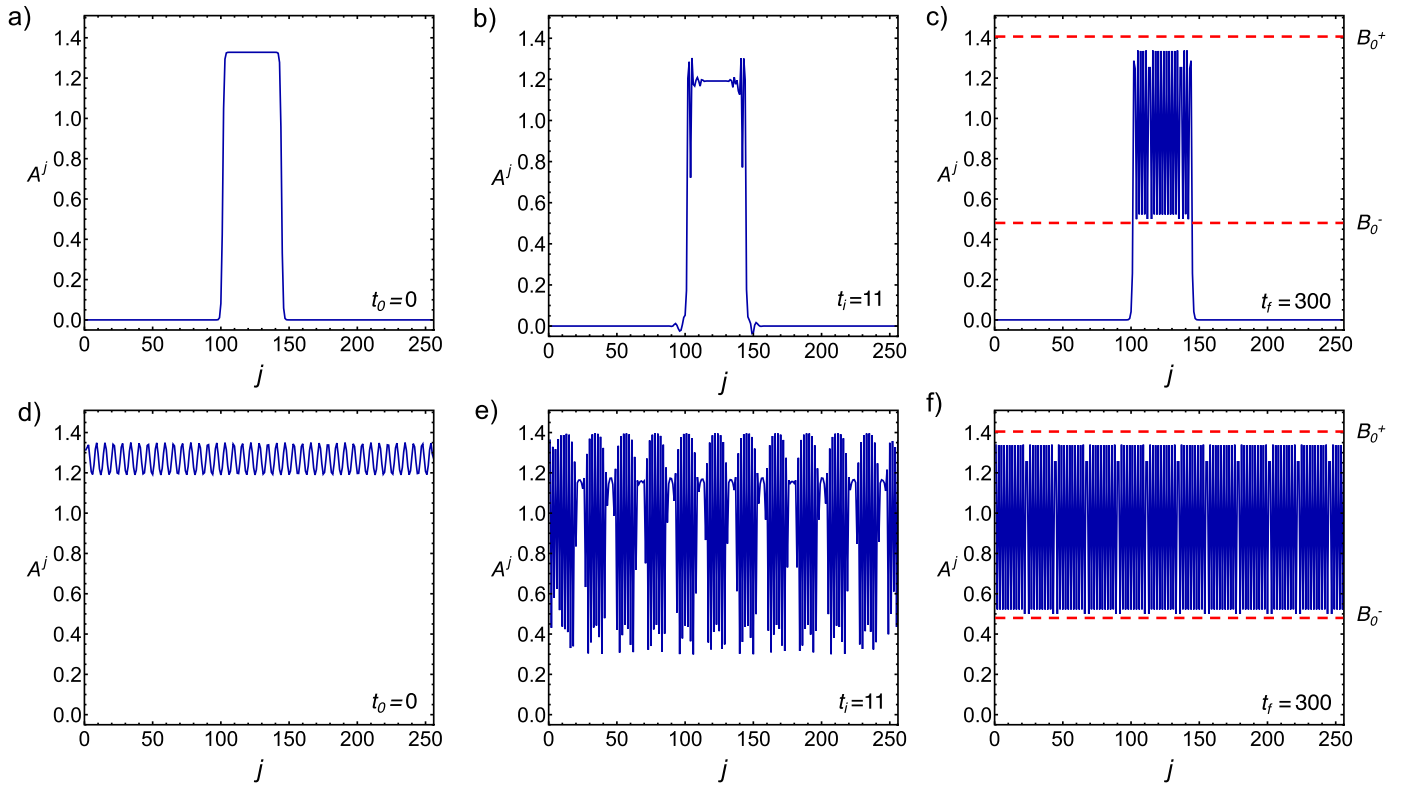


Fig. 2. Localized disorder state. Panels (a), (b), and (c) display the input, transient, and established localized states, generated by simulations of Eq. (1) with $\epsilon = 0.51$, $\alpha = 0.35$, $\gamma = 1.01$, and $\nu = -1.15$ at three instants of time $t_0 = 0$, $t_i = 11$, and $t_f = 300$. Panels (d), (e), and (f) display the corresponding solutions for the extended state that occupies the entire spatial domain at the same value of the parameters. Both the localized and extended states are filled by the LW (leaping wave). The red lines represent CW amplitudes described by Eq. (7) for the given values of α , γ , and ν . (For interpretation of the references to color in this figure legend, the reader is referred to the web version of this article.)

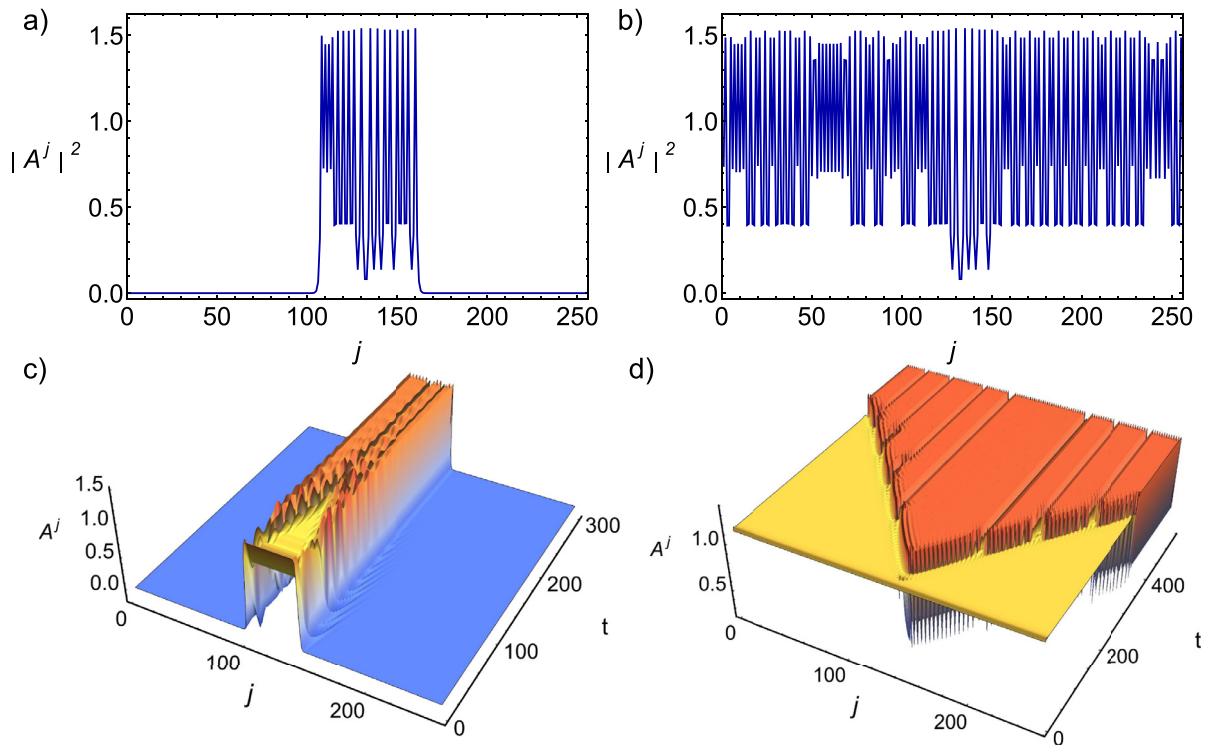


Fig. 3. Disordered localized state. Panels (a) and (b) show the squared absolute value, $|A^j|^2$, for the robust confined localized state and the extended one, respectively, filled by the LW (leaping wave). Panels (c) and (d) show the spatiotemporal evolution of $\text{Re}(A^j(t))$ from the flat-amplitude inputs towards the final states depicted in (a) and (b), respectively. The solutions are produced by Eq. (1) at $\gamma = 0.55$, $\nu = -1.0$ with $\alpha = 0.35$ and $\epsilon = 0.51$.

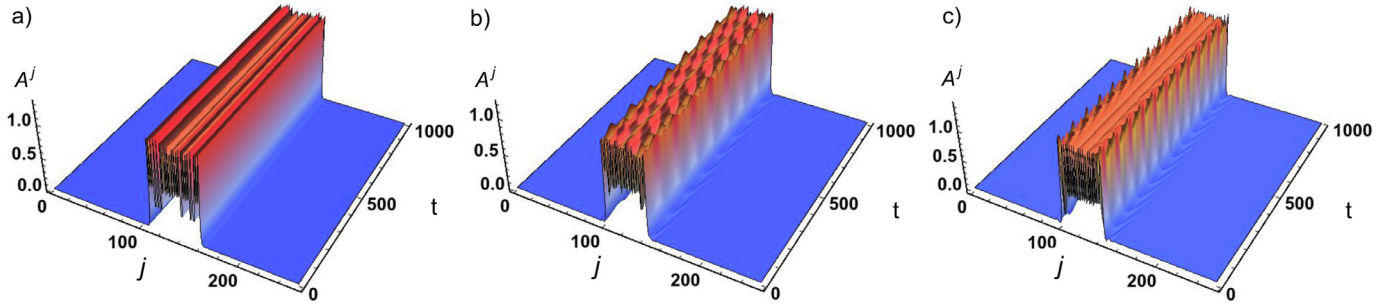


Fig. 4. Chimera states. Spatiotemporal evolution of $\text{Re}(A^j(t))$ for three species of self-confined chimera states, generated by simulations of Eq. (1). (a) A disorder localized state, found for $\gamma = 0.67$, $\nu = -1.0$, with $\lambda_{\max} = -0.011$. (b) A quasi-periodic chimera, for $\gamma = 0.75$ and $\nu = -0.80$, with $\lambda_{\max} = -5.54 \times 10^{-5}$. (c) A chaotic chimera, for $\gamma = 0.90$ and $\nu = -1.2$, with $\lambda_{\max} = 0.07$.

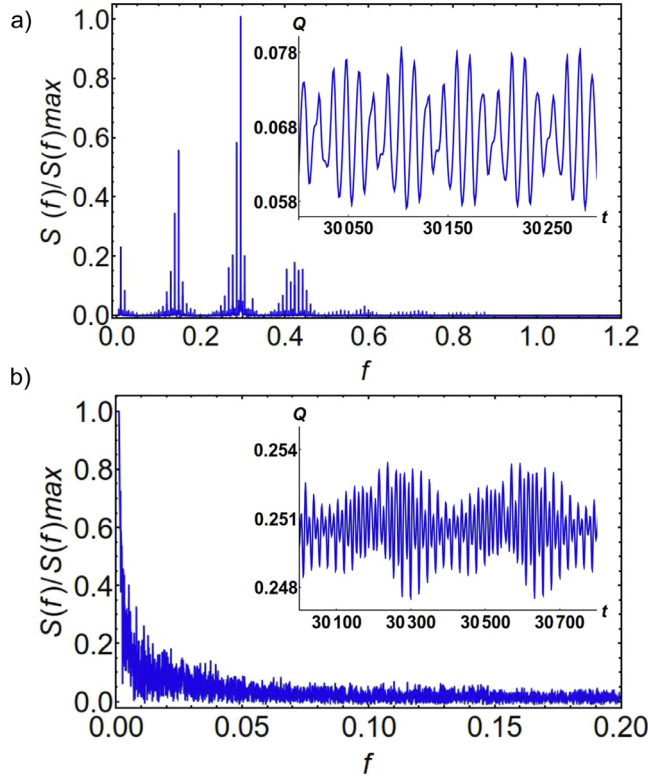


Fig. 5. The power spectrum, $S(f)$, of the time-dependent total norm, $Q(t)$, defined as per Eq. (27). Panels (a) and (b) correspond to the quasi-periodic and chaotic chimeras, displayed in Fig. 4(b) and (c), respectively. The corresponding time dependences $Q(t)$ [see Eq. (26)] are displayed in the insets.

The substitution of ansatz (15) in Eq. (14) yields a dispersion equation for $\sigma(k)$

$$\sigma(\sigma + 2\alpha) + [4\epsilon \sin^2(k/2) \mp 2\gamma \sin(2\delta) + 2\nu] \times [4\epsilon \sin^2(k/2) \mp 2\gamma \sin(2\delta)] = 0. \quad (16)$$

It is easy to see that the continuum limit of Eq. (16), which is defined as per Eq. (6), always gives rise to instability (represented by a root with $\sigma > 0$). On the other hand, the analysis reveals a region in the parameter space in which Eq. (16) secures stability of the CW in the above-mentioned relevant case, with $\nu < 0$ and the top sign in Eqs. (2), (7), and (16)

$$\alpha^2 + 4\epsilon^2 \equiv (\gamma_{\min}^2)_{\text{CW}} < \gamma^2 < \alpha^2 + \nu^2 \equiv \gamma_{\max}^2. \quad (17)$$

The self-consistency condition for the double inequality in Eq. (17) is $\epsilon < |\nu|/2$. Here the left inequality is the CW modulational-stability condition proper, while the right one is

copied from the top line of Eq. (5). Therefore, the CW state (2) with amplitude $B_0^{(+)}$ and zero solution are *simultaneously stable* in the parameter window defined by Eq. (17). The possibility of the respective *bistability* is relevant to the present work, which aims to build up stable nonzero modes on top of the stable zero background (although, as shown above, these two stable states cannot be connected by a transient-layer solution).

On the other hand, straightforward consideration of Eq. (16) demonstrates that, in the same case, the CW state with smaller amplitude, which corresponds to the bottom sign in Eqs. (2), (7), and (16), is always subject to the modulational instability. Another obvious corollary of Eq. (17) is that (as it is well known [84]) the stability interval (17) does not exist in the absence of the drive and damping, $\gamma = \alpha = 0$.

2.5. Staggered states

In addition to the stationary solutions with the fixed phase considered above in the form of ansatz (2), it is possible to introduce *staggered solutions* of Eq. (1), with alternating signs of amplitudes at adjacent sites of the lattice, $A^j \equiv (-1)^j \tilde{A}^j$. This transformation casts Eq. (1) in the form of

$$\begin{aligned} \frac{d\tilde{A}^j}{dt} &= i\epsilon(\tilde{A}^{j+1} + \tilde{A}^{j-1} + 2\tilde{A}^j) - i|\tilde{A}^j|^2\tilde{A}^j \\ &\quad - i\nu\tilde{A}^j + \gamma(\tilde{A}^j)^* - \alpha\tilde{A}^j. \end{aligned} \quad (18)$$

Further, the substitution of

$$\tilde{A}^j = \tilde{B}^j \exp(\mp i\delta_0), \quad (19)$$

with the same δ_0 as in Eq. (2) and real discrete field \tilde{B}^j , leads to the respective stationary equation,

$$\begin{aligned} -\epsilon(\tilde{B}^{j+1} + \tilde{B}^{j-1} + 2\tilde{B}^j) + (\tilde{B}^j)^3 = \\ (-\nu \pm \sqrt{\gamma^2 - \alpha^2})\tilde{B}^j. \end{aligned} \quad (20)$$

Solutions to Eqs. (18) and (20) can be obtained from the above un-staggered ones by substitution

$$\epsilon \rightarrow -\epsilon, \nu \rightarrow \nu - 4\epsilon. \quad (21)$$

In particular, a solution to Eq. (20) with constant \tilde{B}^j gives rise to the following staggered version of the CW state, which can be obtained from the CW solution (7) via substitution (21) (the solution is written here in terms of the original lattice field A^j , rather than \tilde{A}^j):

$$A^j = (-1)^j \sqrt{4\epsilon - \nu \pm \sqrt{\gamma^2 - \alpha^2}} \exp(\mp i\delta_0). \quad (22)$$

Two different solutions given by Eq. (22) with opposite signs \pm exist if, as above, condition $\gamma > \alpha$ holds, and the intersite coupling

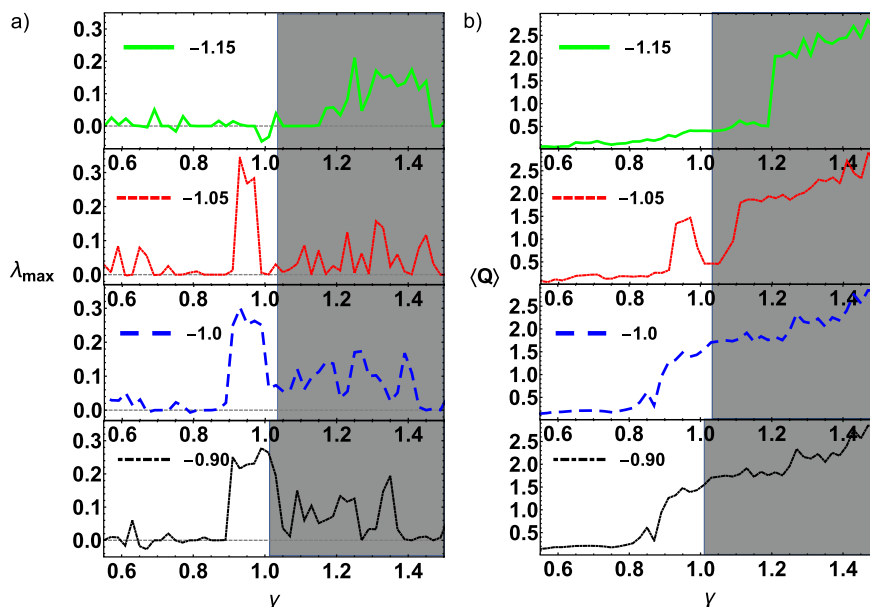


Fig. 6. Dynamical indicators. (a) LLE and (b) time-average of the total norm (Q) as functions of γ for fixed negative values of ν , which are indicated in the panels. Other parameters in Eq. (1) are $\mu = 0.35$, $\epsilon = 0.51$, and $\alpha = 0.35$. In shaded areas the stationary LW (leaping wave), filling the entire lattice, is unstable.

strength is subject to constraint

$$\epsilon > (1/4) \left(\nu + \sqrt{\gamma^2 - \alpha^2} \right). \quad (23)$$

In particular, for $\nu < 0$ condition (23) holds if γ satisfies inequality (8), the same one which is necessary for the coexistence of two unstaggered CWs given by Eqs. (2) and (7).

Further, staggered decaying-tail solutions of the linearized version of Eq. (20), in the form of $\tilde{B}^j = \tilde{b}_0 \exp(-q|j|)$, which make possible to connect zero and nonzero states [cf. Eq. (9)], are obtained from Eq. (10) with the help of substitution (21):

$$\cosh^2(q/2) = (4\epsilon)^{-1} \left(\nu \mp \sqrt{\gamma^2 - \alpha^2} \right), \quad (24)$$

while the stability conditions for the zero solution keep the form of Eq. (5). In the case of $\nu < 0$ (negative detuning), the tail solution (24) exists solely under condition $\gamma^2 > \alpha^2 + \nu^2$, which makes the zero state unstable, as per the top line in Eq. (5). Hence, the staggered CW solution cannot coexist with stable zero, as parts of a chimera or localized state. In the case of positive detuning, $\nu > 0$, a possibility of building a chimera combining the stable zero and a stable staggered CW is not promising either, because conditions necessary for the existence of tail (24), i.e., $\cosh^2(q/2) > 1$, and of two CW states, as given by Eq. (22), contradict each other.

Lastly, as a generalization of the staggered solutions, it is possible to introduce “twisted” ones (so named following Ref. [85]), in which stationary field B^j [defined as in Eq. (2)] takes opposite values at sites separated by ones with $B^j = 0$:

$$B^j = \begin{cases} \sqrt{2\epsilon - \nu \pm \sqrt{\gamma^2 - \alpha^2}}, & j = 4n, \\ 0, & j = 1 + 2n, \\ -\sqrt{2\epsilon - \nu \pm \sqrt{\gamma^2 - \alpha^2}}, & j = 2(1 + 2n), \end{cases} \quad (25)$$

cf. Eqs. (7) and (22). In this work, we do not aim to consider patterns of this type in detail.

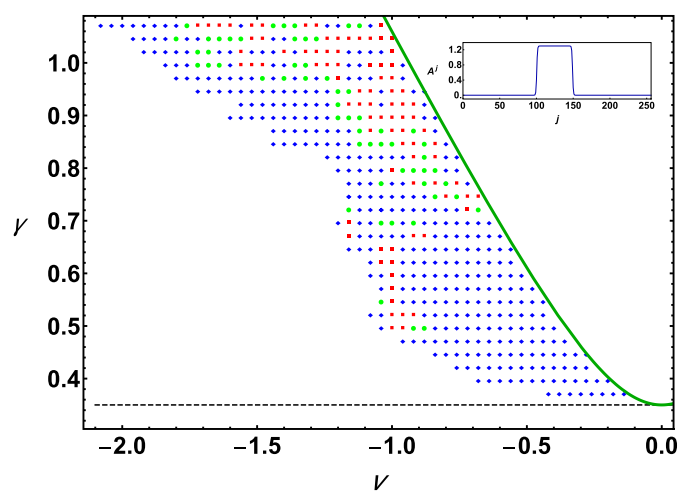


Fig. 7. Different species of robust self-confined states, generated by simulations of Eq. (1) with the same localized input (shown in the inset), are chartered in the parameter plane of the detuning, ν , and parametric-drive's strength, γ , for a fixed inter-site coupling constant, $\epsilon = 0.51$, and the value of the dissipation coefficient fixed by the rescaling, $\alpha = 0.35$. Blue diamonds, green circles, and red squares represent, respectively, stable localized disorder state, chimera with quasi-periodic evolution, and chaotic spatiotemporal dynamics in the spatially confined area. The dashed horizontal line, $\gamma = \alpha \equiv 0.35$, is the boundary above which two CW states (7) exist at $\nu < 0$. Only the CW state may exist, as a stable one, above the green continuous curve, i.e., at $\gamma > \gamma_{\max} = \alpha^2 + \nu^2$ [see the top line in Eq. (5)], where the zero solution and, hence, any finite-width chimera as a whole are unstable. Indeed, for $\alpha = 0.35$ and $\epsilon = 0.51$, the stable CW exists at $\gamma > \sqrt{\alpha^2 + 4\epsilon^2} \approx 1.08$ [as per the left-hand inequality in Eq. (17)], i.e., above the area displayed in the present figure. No stable nonzero states are produced by the simulations in the white area to the left of the filled region. (For interpretation of the references to color in this figure legend, the reader is referred to the web version of this article.)

3. Localized states

3.1. Localized disorder states

The underlying Eq. (1) with the above-mentioned boundary conditions was solved by means of a variable-step fifth-order Runge-Kutta scheme that ensures the relative precision of 10^{-7}



Fig. 8. Existence regions of different stable states as a function of the intersite coupling constant, ϵ , at fixed values of the drive's strength, $\gamma = 0.95$, and detuning, $\nu = -1.11$. The localized states (localized disorder and chimeras) are stable in the interval of $0.44 < \epsilon < 0.81$. At $\epsilon < \epsilon_{\text{crit}} \approx 0.44$ [see Eq. (30)], stable states, depending on the initial conditions, are uniform CWs or broad flat patches of CWs, bounded by narrow transient layers with sharp (but low) peaks, see Fig. 9. At $\epsilon > 0.81$, Eq. (1) gives rise to stable delocalized patterns with zero crossings (not considered here in detail).

[91]. The integration was performed up to $t = 4.8 \times 10^3$, which is essentially larger than the sufficient time for the establishment of various static and dynamical states. To identify the region of existence of chimera states, we have first produced stable patterns filling the entire solution domain. Then, the numerical solution produced chimeras by taking parameters from the patterns' stability area, and running simulations of Eq. (1) with inputs in the form of a localized segment of the extended pattern, set in the central part of the integration domain. The same localized states could be produced from a simpler input, taken as a rectangular box with a constant amplitude in a central segment of the integration domain, letting it evolve into a static or dynamical chimera of approximately the same width, see an example below in Fig. 4(c).

The forcing, damping, and detuning terms play a crucial role in the formation of various states in the present model. As said above, the damping coefficient is fixed to be constant through rescaling, $\alpha = 0.35$, therefore results were collected by varying γ and ν , while (in most cases) the intersite coupling constant was kept constant, at value $\epsilon = 0.51$, which allows to present generic findings.

Fig. 2 shows examples of stationary states, produced as numerical solutions of Eq. (1) with $\gamma = 1.01$ and $\nu = -1.15$. Panel (a) displays the above-mentioned input, taken as a rectangular box with a flat amplitude. Panel (b) represents a transient state produced in the course of the evolution, that leads to the establishment of the stationary localized disorder depicted in panel (c). It is a finite-length patch of a quasi-regular LW separated by steep edges (fronts) from the zero state. This localized disorder state is stable and motionless at the present values of the parameters, according to the top line in Eq. (5).

Further, panel (f) displays a stationary LW pattern occupying the entire integration domain, obtained via an intermediate state (panel e)) from the input shown in panel (d). It was introduced as a small-amplitude periodic wave with the mean value close to the CW amplitude B_0^+ , given by Eq. (7) for current values of the parameters: $B_0^{(+)} \approx 1.448$ and $B_0^{(-)} \approx 0.450$. The periodic component was added to the input to initiate the development of the extended LW state. Note that both values $B_0^{(\pm)}$ are clearly visible as the limits, shown by red lines in panels (c) and (f), between which the LW oscillates in both the confined (localized disorder state) and extended states. The numerical data demonstrate that the stationary solutions displayed in panels (c) and (f) have a spatially uniform phase.

Similar dynamics is observed at other values of the parameters. In particular, Fig. 3 displays the full picture of the establishment of the patch-shaped (localized disorder state) state with the LW structure, and its counterpart filling the entire domain, at $\gamma = 0.55$, $\nu = -1.0$, $\alpha = 0.35$, and $\epsilon = 0.51$. Fig. 3(c) and (d) corroborate the modulational instability of the above-mentioned CW state, with $B_0^{(+)} \approx 1.448$, in the confined and fully extended forms alike, in agreement with the fact that the current parameter values do not satisfy the left-side inequality in the CW stability condition given by Eq. (17). The observation that the instability onset and

development are essentially the same in panels (c) and (d) is explained by the fact that the instability maximum determined by Eq. (16) corresponds to $k = \pi$, hence the corresponding perturbation wavelength, $2\pi/k = 2$, is much smaller than the width of the initial CW domains in both panels.

Another essential conclusion suggested by Figs. 2 and 3 is that a sharp edge separating the zero and nonzero parts of the finite-size patch (localized state) is always stable, which makes it possible to build up a stationary localized disorder state of an arbitrary size, confined by a pair of edges. Thus, the system demonstrates multistability, including localized states of different sizes, as well as configurations with two or several localized domains separated by zero-amplitude segments (not shown here).

3.2. Dynamical indicators

To characterize different nature of dynamical behavior of localized states, we use, first, the scaled total norm, which (along with the Hamiltonian) is a dynamical invariant of the DNLS equation in the absence of the damping and drive [58], while in the present case it is a function of time, in non-stationary states:

$$Q(t) = \frac{1}{N} \sum_{j=1}^N |A^j(t)|^2. \tag{26}$$

In the case of time-dependent $Q(t)$, we computed its power spectrum,

$$S(f) = |\mathfrak{F}(f)|^2, \tag{27}$$

as a function of frequency f [related to the angular frequency as $f = \omega/(2\pi)$], where the Fourier transform of $Q(t)$ is defined as

$$\mathfrak{F}(f) = \frac{1}{\sqrt{2\pi}} \int_0^{t_{\text{max}}} Q(t) \exp(-ift) dt. \tag{28}$$

A general principle is that $S(f)$ features a quasi-discrete spectrum, with a set of narrow peaks, for regular solutions, which exhibit (quasi-) periodic evolution in time. On the other hand, the spectrum is expected to be an essentially continuous one if the underlying time-dependent solution can be of chaotic nature [92], see also a recent realization of the principle for the nonlinear Schrödinger equation with a trapping potential [93].

Another relevant indicator characterizing the dynamical behavior is the *largest Lyapunov exponent* (LLE), λ_{max} [92,94]. When the system is chaotic, two trajectories, that were infinitesimally close initially, separate in the phase space exponentially, the distance between them growing $\sim \exp(\lambda_{\text{max}}t)$, with $\lambda_{\text{max}} > 0$. On the other hand, close trajectories converge to the same non-chaotic attractor if $\lambda_{\text{max}} < 0$. The marginal case of $\lambda_{\text{max}} = 0$ implies that the behavior is time-periodic, quasi-periodic, or complex behavior with power sensitivity to initial conditions. LLE is widely used to quantify regular and chaotic evolution in diverse dynamical systems, see, e.g., Refs. [94–102].

3.3. Chimera states

To collect systematic numerical data, we ran simulations of model Eq. (1) with the initial state in the form of a state with a flat amplitude, filling a central segment of the integration domain, as shown above in Figs. 2(a) and 3(c). Generic results, obtained at different values of the driving strength, γ , and negative detuning, ν , are displayed in Fig. 4, in the form of established dynamical regimes, observed in the course of a long simulation interval, $0 < t < 1000$. All these self-sustained states were created in a finite lattice segment, $100 < j < 160$.

In panel 4(a), the evolution at $\gamma = 0.67$ and $\nu = -1.0$ leads to the establishment of a stable time-independent localized disorder

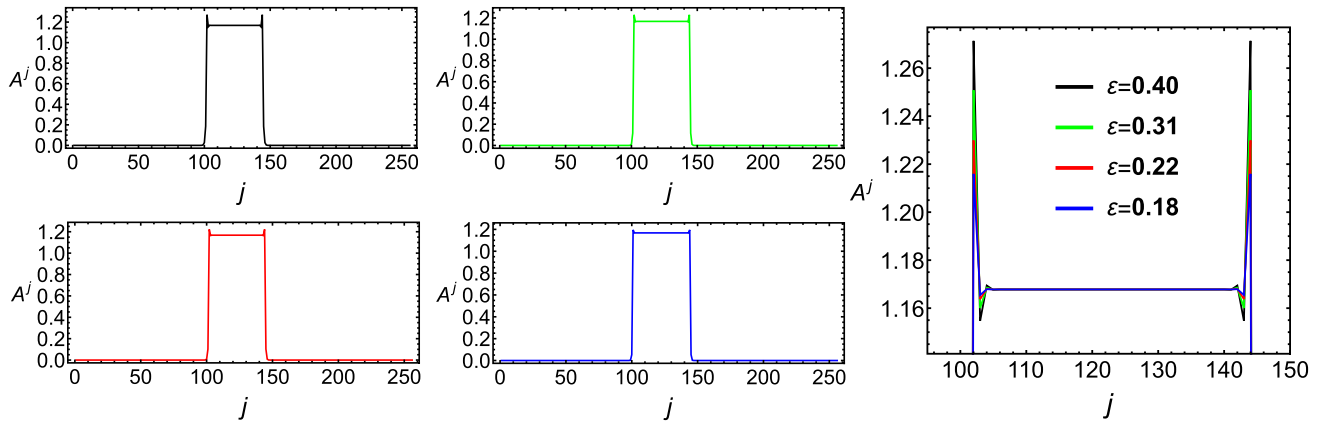


Fig. 9. $\text{Re}(A^j)$ for stable states in the form of confined flat (CW) patches, bounded by narrow layers with sharp peaks. The states are obtained at $\gamma = 0.95$, $\nu = -1.11$, and $\alpha = 0.35$ (the same as in Fig. 8), with $\epsilon = (0.40, 0.31, 0.22, 0.18)$, as color coded in the right panel (which provides a zoom of the sharp peaks). Note that all these values of the lattice coupling constant belong to the region (30).

state. In this case, the respective value given by the top line in Eq. (5) is $\gamma_{\max} \approx 1.06$, hence the zero background is indeed stable. The regular behavior of this localized state as a whole is corroborated by the computation of the respective LLE, which is found to be negative, $\lambda_{\max} = -0.011$.

Next, increasing the strength of the forcing, a chimera featuring quasi-periodic temporal dynamic is displayed in panel 4(b) for $\gamma = 0.75$ and $\nu = -0.80$, which is closer to the respective stability boundary for the zero state, viz., $\gamma_{\max} \approx 0.87$, as per the top line in Eq. (5). Notice that this solution accounts for a coexistence of coherent and incoherent domains. In this case, LLE is $\lambda_{\max} = -5.54 \times 10^{-5} \pm 5.72 \times 10^{-6}$, which is actually a numerical zero, as may be expected for quasi-periodic states. Finally, a chaotic chimera, featuring apparently random spatiotemporal dynamic at $\gamma = 0.90$ and $\nu = -1.2$ in a self-confined segment of the lattice, is displayed in panel (c). In the latter case, Eq. (5) yields $\gamma_{\max} \approx 1.25$, hence the zero background remains stable. The numerically computed LLE is positive, $\lambda_{\max} = 0.07$, which clearly corroborates the chaotic character of the state as a whole [92].

To gain deeper understanding of the dynamics, the quasi-periodic and chaotic character of the chimeras displayed in Fig. 4(b) and (c) is quantified by the corresponding power spectra, defined as per Eq. (27), which are presented in Fig. 5(a) and (b), respectively. As expected, the spectrum is quasi-discrete for the quasi-periodic oscillations and continuous for the chaotic dynamics. The previous analysis allows us to conclude that the emergence of quasi-periodic and chaotic chimeras follows a route of extended quasi-periodicity [103].

The effect of the strength of the parametric forcing, γ , on properties of the states under the consideration is represented by Fig. 6, which shows LLE and the time-average value of the total norm,

$$\langle Q \rangle = t_{\max}^{-1} \int_0^{t_{\max}} Q(t) dt, \quad (29)$$

as functions of γ , at different fixed values of detuning parameter ν , for the self-confined states created in the above-mentioned lattice segment, $100 < j < 160$. The transition from regular to chaotic dynamic with the increase of the forcing strength, γ , i.e., from $\lambda_{\max} \approx 0$ to definitely positive values of λ_{\max} , coincides with the transition from nearly constant to growing values of $\langle Q \rangle$. Both phenomena are manifestations of the phase transition from regular dynamic to chaos, which takes place at a critical point, $\gamma = \gamma_{\text{crit}}$. For example, $\gamma_{\text{crit}}(\nu = -0.90) \approx 0.92$ and $\gamma_{\text{crit}}(\nu = -1.05) \approx 0.90$, while the respective values given by Eq. (5) are $\gamma_{\max}(\nu = -0.9) \approx 0.966$ and $\gamma_{\max}(\nu = -1.05) \approx 1.107$ [recall we have fixed the dissi-

pation constant in Eq. (1) as $\alpha = 0.35$, by means of scaling]. Thus, the transition to the chaotic dynamic happens when the zero state is still stable, at $\gamma < \gamma_{\max}$. Generally, ratio $\gamma_{\text{crit}}/\gamma_{\max}$ takes values between 0.81 and 0.90.

Moreover, in the shaded area in Fig. 6 direct simulations demonstrate that the extended LW state is unstable. Thus, in an interval of the drive's strength between γ_{crit} and the left edge of the shaded area the dynamic is categorized as chaotic, while the explicit LW instability does not set in, as yet. The "delay" of the onset of the instability after the transition to the positive LLE may be a consequence of the finite width of the self-confined patch (localized state) filled by LW. Finally, stable CWs are easily found at $\gamma > (\gamma_{\min})_{\text{CW}}$, where, for the current values of the parameters, $\alpha = 0.35$ and $\epsilon = 0.51$, the left-hand inequality in Eq. (17) gives $(\gamma_{\min})_{\text{CW}} \approx 1.08$.

Results of the systematic numerical analysis are summarized in Fig. 7, which is a chart designating different established states in the parameter plane of (ν, γ) . The states are categorized, with the help of the value of LLE, λ_{\max} , and the character of the power spectrum of $Q(t)$ (quasi-discrete or continuous), as stationary, temporarily quasi-periodic, or chaotic self-confined chimeras (blue diamonds, green circles, and red squares, respectively, in Fig. 7). The results were generated by means of sufficiently long simulations of Eq. (1), initiated, at all values of ν and γ , by the rectangular excitation field displayed in the inset to Fig. 7. The localized states, which include extended segments of the stable zero solution, exist between the dashed horizontal line, $\gamma = \alpha = 0.35$, and the solid green curve, $\gamma = \gamma_{\max}$ [see the top line in Eq. (5)]. These boundaries correspond, respectively, to the above-mentioned saddle-node and inverse pitchfork bifurcations. In particular, at values of the drive's strength $\gamma < 0.48$ and $0.55 < \gamma < 0.65$ for $\nu > -1.0$ the chart contains only stationary chimeras.

We stress that the model obviously features multistability, as different species of the stable state coexist at the same values of the parameters. In particular, as mentioned above (see Figs. 2–4), Eq. (1) admits bistability between localized and delocalized states, which are readily found as stable solutions at the same values of the parameters, the choice between them being determined by the initial conditions.

The above results were obtained for the fixed value of the intersite coupling constant, $\epsilon = 0.51$. It is also relevant to consider effects of variation of ϵ . In Fig. 8 we report the results for fixed $\gamma = 0.95$ and $\nu = -1.11$, the respective value given by the top line of Eq. (5) being $\gamma_{\max} \approx 1.16$. The figure demonstrates that, at $\epsilon < 0.44$, the simulations produce no chimeras, which are ousted

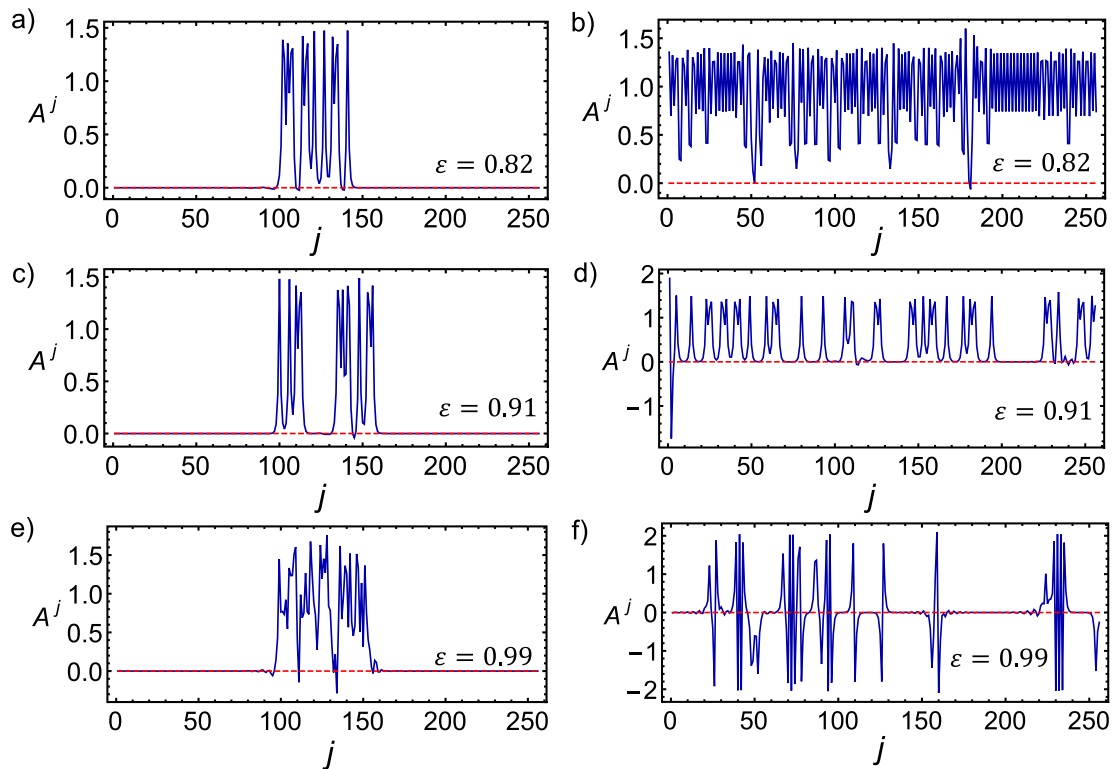


Fig. 10. Stable randomly shaped patterns produced by the simulations at the same fixed values of the parameters, $\gamma = 0.95$, $\nu = -1.11$, and $\alpha = 0.35$, as in Figs. 8 and 9. The patterns are produced at gradually increasing values of the lattice coupling constant, ϵ , which leads to deeper zero crossing. The left and right columns display, severally, confined and extended patterns, produced by respective inputs.

by the stable uniform CW, in exact agreement with the left-hand inequality in Eq. (17), which shows that CWs are stable at

$$\epsilon < \epsilon_{\text{crit}} \equiv (1/2)\sqrt{\gamma^2 - \alpha^2} \approx 0.44, \tag{30}$$

for $\gamma = 0.95$ and $\alpha = 0.35$. Detailed simulations demonstrated that, in the same region at $\epsilon < \epsilon_{\text{crit}}$, the established numerical solution depends on initial conditions. If an extended pattern is taken as the input, simulations establish a uniform CW with amplitude B_0^+ , see Eq. (7). On the other hand, the input in the form of a localized region filled by the LW gives rise to robust solutions in the form of wide but confined flat CW patches, which are bounded by narrow transient layers including sharp (but relatively low) peaks, such as the ones shown in Fig. 9. Because of the presence of the peaks, these states cannot be predicted by ansatz (11) considered above. The right panel on Fig. 9 demonstrates that the height of the peaks diminishes with the decrease of ϵ .

As shown in Fig. 8, for the same fixed values $\gamma = 0.95$ and $\nu = -1.11$, stable finite-width chimeras are produced by numerical simulations in an interval of values of the coupling constant $0.44 < \epsilon < 0.81$. Lastly, at $\epsilon > 0.81$, the former chimera patterns acquire zero points (originally falling to $A_j = 0$, and then crossing zero), as shown in Fig. 10. However, these states are different from the zero-crossing twisted ones, given by Eq. (25), as they are apparently randomly built patterns. As shown in Fig. 10, they may feature both confined and extended shapes, depending on the input.

4. Conclusion

In this work, we have presented chimera states and localized disordered states found in the parametrically driven discrete dis-

sipative system, modeled by the damped DNLS equation with the onsite parametric drive. The system can be implemented as an array of optical fibers in which losses are compensated by the parametric amplification. The localized states are built as finite segments filled by a pattern which may be a stationary LW (a spatially *leaping wave* oscillating between lattice sites), or, depending on parameters, an LW featuring quasi-periodic or chaotic time dependence. The segment is connected by steep fronts to stable zero states (in this sense, it is a chimera combining stable nonzero and zero modes). The dynamics of the chimeras is characterized by the time dependence of the total norm, and by LLE (the largest Lyapunov exponent). Our analysis reveals a specific region of parameters in which robust localized disordered and chimera states exist, the strength and detuning of the parametric drive being the essential control parameters. The dependence of the existence region on the strength of the intersite coupling, ϵ , is considered as well. Besides, for smaller values of ϵ , stable states are represented by flat CW patches, which are confined by narrow transient layers containing sharp peaks. A part of the numerical findings is explained by analytical results that address the existence and stability of the zero and uniform CW states.

As an extension of the analysis, it may be relevant to consider chimera states in the two-dimensional version of the present system. Work in this direction is in progress.

Declaration of Competing Interest

The authors declare that they have no known competing financial interests or personal relationships that could have appeared to influence the work reported in this paper.

Acknowledgments

LMP, PD, and DL acknowledge partial financial support from FONDECYT 1180905. DL acknowledges the partial financial support from Centers of excellence with BASAL/CONICYT financing, Grant AFB180001, CEDENNA. The work of BAM is supported, in a part, by the Israel Science Foundation, through grant no. 1286/17. This author appreciates hospitality of Instituto de Alta Investigación at Universidad de Tarapacá (Arica, Chile). MGC thanks for the financial support FONDECYT projects 1180903 and Millennium Institute for Research in Optics ANID-Millennium Science Initiative Program–ICN17_012.

References

- [1] Kuramoto Y. Chemical oscillations, waves, and turbulence. Berlin, Heidelberg: Springer-Verlag; 1984.
- [2] Braun OM, Kivshar Y. The Frenkel–Kontorova, model concepts, methods, and applications. Berlin, Heidelberg: Springer-Verlag; 2004.
- [3] Remoissenet M. Waves called solitons concepts and experiments. Berlin: Springer Science & Business Media; 2013.
- [4] Ablowitz MJ, Ablowitz MA, Prinari B, Trubatch AD. Discrete and continuous nonlinear Schrödinger systems. Cambridge: Cambridge University Press; 2004.
- [5] Kosevich AM. The crystal lattice. Weinheim: Wiley VCH.; 1999.
- [6] Kaneko K, Tsuda I. Chaos and beyond a constructive approach with applications in life sciences. Berlin: Springer; 1996.
- [7] Pikovsky A, Rosenblum M, Kurths J, Hilborn RC. Synchronization a universal concept in nonlinear sciences. Cambridge University Press; 2002.
- [8] Kuramoto Y, Battogtokh D. Coexistence of coherence and incoherence in nonlocally coupled phase oscillators. Nonlinear Phenom Complex Syst 2002;5:380.
- [9] Abrams DM, Strogatz SH. Chimera states for coupled oscillators. Phys Rev Lett 2004;93:174102.
- [10] Faghania Z, Araba Z, Parasteha F, Jafaria S, Perc M, Slavinec M. Effects of different initial conditions on the emergence of chimera states. Chaos Solitons Fractals 2018;114:306.
- [11] Rybalova EV, Vadvivasova TE, Strelkova GI, Anishchenko VS, Zakharova AS. Forced synchronization of a multilayer heterogeneous network of chaotic maps in the chimera state mode. Chaos 2019;29:033134.
- [12] Clerc MG, Ferré MA, Coulibaly S, Rojas RG, Tlidi M. Chimera-like states in an array of coupled-waveguide resonators. Opt Lett 2017;42:15.
- [13] Kemeth FP, Haugland SW, Schmidt L, Kevrekidis IG, Krischer K. A classification scheme for chimera states. Chaos 2016;26:094815.
- [14] Omel'chenko OE, Maistrenko YL, Tass PA. Chimera states the natural link between coherence and incoherence. Phys Rev Lett 2008;100:044105.
- [15] Laing CR. Chimera states in heterogeneous networks. Chaos 2009;19:013113.
- [16] Omel'chenko OE, Wolfrum M, Maistrenko YL. Chimera states as chaotic spatiotemporal patterns. Phys Rev E 2010;81:065201(R).
- [17] Omel'chenko OE, Maistrenko Y, Hövel P, Schöll E. Loss of coherence in dynamical networks spatial chaos and chimera states. Phys Rev Lett 2011;106:234102.
- [18] Wolfrum M, Omel'chenko OE, Yanchuk S, et al. Spectral properties of chimera states. Chaos 2011;21:013112.
- [19] Lee WS, Restrepo JG, Ott E, Antonsen TM. dynamic and pattern formation in large systems of spatially-coupled oscillators with finite response times. Chaos 2011;21:023122.
- [20] Tinsley MR, Nkomo S, Showalter K. Chimera and phase-cluster states in populations of coupled chemical oscillators. Nat Phys 2012;8:662.
- [21] Hagerstrom AM, Murphy TE, Roy R, Hövel P, Omel'chenko I, Schöll E. Experimental observation of chimeras in coupled-map lattices. Nat Phys 2012;8:658.
- [22] Larger L, Penkovsky B, Maistrenko Y. Virtual chimera states for delayed-feedback systems. Phys Rev Lett 2013;111:054103.
- [23] Nkomo S, Tinsley MR, Showalter K. Chimera states in populations of nonlocally coupled chemical oscillators. Phys Rev Lett 2013;110:244102.
- [24] Sethia GC, Sen A. Chimera states the existence criteria revisited. Phys Rev Lett 2014;112:144101.
- [25] Panaggio MJ, Abrams DM. Chimera states coexistence of coherence and incoherence in networks of coupled oscillators. Nonlinearity 2015;28:R67.
- [26] Bercé V. Chimera state and route to explosive synchronization. Chaos Solitons Fractals 2016;86:75.
- [27] Santos M, Szezech J, Borges F, Iarosz K, Caldasci I, Batista A, et al. Chimera-like states in a neuronal network model of the cat brain. Chaos Solitons Fractals 2017;101:86.
- [28] Guo S, Dai Q, Cheng H, Li H, Xie F, Yang J. Spiral wave chimera in two-dimensional nonlocally coupled Fitzhugh–Nagumo systems. Chaos Solitons Fractals 2018;114:394.
- [29] Parasteh F, Jafari S, Azarnoush H, Shahriari Z, Wang Z, Boccaletti S, Perc M. Chimeras. Phys Rep 2021;898:1.
- [30] Haugland S.W. The changing notion of chimera states, a critical review. 2021. arXiv:2102.05515
- [31] Barashenkov IV, Bogdan MM, Korobov VI. Stability diagram of the phase-locked solitons in the parametrically driven, damped nonlinear Schrödinger equation. Europhys Lett 1991;15:113.
- [32] Barashenkov IV, Zemlyanaya EV. Stable complexes of parametrically driven, damped nonlinear Schrödinger solitons. Phys Rev Lett 1999;83:2568.
- [33] Alexeeva NV, Barashenkov IV, Tsironis GP. Impurity-induced stabilization of solitons in arrays of parametrically driven nonlinear oscillators. Phys Rev Lett 2000;84:3053.
- [34] Barashenkov IV, Alexeeva NV, Zemlyanaya EV. Two- and three-dimensional oscillons in nonlinear faraday resonance. Phys Rev Lett 2002;89:104101.
- [35] Zemlyanaya EV, Alexeeva NV. Oscillating solitons of the driven, damped nonlinear Schrödinger equation. Theor Math Phys 2009;159:870.
- [36] Couillet P, Firsch T, Sonnino G. Dispersion-induced patterns. Phys Rev E 1994;49:2087.
- [37] Barashenkov IV, Zemlyanaya EV, van Heerden TC. Time-periodic solitons in a damped-driven nonlinear Schrödinger equation. Phys Rev E 2011;83:056609.
- [38] Urzagasti D, Laroze D, Clerc MG, Pleiner H. Breather soliton solutions in a parametrically driven magnetic wire. Europhys Lett 2013;104:40001.
- [39] Urzagasti D, Laroze D, Clerc MG, Coulibaly S, Pleiner H. Two-soliton precession state in a parametrically driven magnetic wire. J Appl Phys 2012;111:07D111.
- [40] Barashenkov IV, Zemlyanaya EV. Soliton complexity in the damped-driven nonlinear Schrödinger equation stationary to periodic to quasiperiodic complexes. Phys Rev E 2011;83:056610.
- [41] Urzagasti D, Aramayo A, Laroze D. Soliton-antisoliton interaction in a parametrically driven easy-plane magnetic wire. Phys Lett A 2014;378:2614.
- [42] Shchesnovich VS, Barashenkov IV. Soliton-radiation coupling in the parametrically driven, damped nonlinear Schrödinger equation. Phys D 2002;164:83.
- [43] Barashenkov IV, Cross S, Malomed BA. Multistable pulse-like solutions in a parametrically driven Ginzburg–Landau equation. Phys. Rev. E 2003;68:056605.
- [44] Clerc MG, Coulibaly S, Laroze D. Localized states beyond the asymptotic parametrically driven amplitude equation. Phys Rev E 2008;77:056209.
- [45] Burke J, Yochelis A, Knobloch E. Classification of spatially localized oscillations in periodically forced dissipative systems. SIAM J Appl Dyn Sys 2008;7:651.
- [46] Kenig E, Malomed BA, Cross MC, Lifshitz R. Intrinsic localized modes in parametrically driven arrays of nonlinear resonators. Phys Rev E 2009;80:046202.
- [47] Clerc MG, Coulibaly S, Laroze D. Nonvariational Ising–Bloch transition in parametrically driven systems. Int J Bifurc Chaos 2009;19:2717.
- [48] Clerc MG, Coulibaly S, Laroze D. Parametrically driven instability in quasi-reversal systems. Int J Bifurc Chaos 2009;19:3525.
- [49] Clerc MG, Coulibaly S, Laroze D. Interaction law of 2D localized precession states. Europhys Lett 2010;90:38005.
- [50] Clerc MG, Coulibaly S, Laroze D. Localized states and non-variational Ising–Bloch transition of a parametrically driven easy-plane ferromagnetic wire. Phys D 2010;239:72.
- [51] Ma Y-P, Burke J, Knobloch E. Defect-mediated snaking a new growth mechanism for localized structures. Phys D 2010;239:1867.
- [52] Clerc MG, Coulibaly S, Laroze D. Localized waves in a parametrically driven magnetic nanowire. Europhys Lett 2012;97:30006.
- [53] Urzagasti D, Laroze D, Pleiner H. Localized chaotic patterns in weakly dissipative systems. Eur Phys J Spec Top 2014;223:141.
- [54] Clerc MG, Coulibaly S, Laroze D, León AO, Nuñez AS. Alternating spin-polarized current induces parametric resonance in spin valves. Phys Rev B 2015;91:224426.
- [55] León AO, Laroze D, Clerc MG, Cabanas AM. Alternating superlattice textures in driven nanomagnets. Commun Nonlinear Sci Numer Simul 2017;44:404.
- [56] Cabanas AM, Clerc MG, Laroze D, León AO. Chaotic patterns and localized states in spin valves. J Magn Magn Mater 2019;476:589.
- [57] Urra H, Marín J, Páez-Silva M, Taki M, Coulibaly S, Gordillo L, García-Núñez MA. Localized faraday patterns under heterogeneous parametric excitation. Phys Rev E 2019;99:033115.
- [58] Kevrekidis PG. Discrete nonlinear Schrödinger equation mathematical analysis. Numerical computations and physical perspectives. New York: Springer; 2009.
- [59] Malomed BA. Nonlinearity and discreteness solitons in lattices. Emerging frontiers in nonlinear science. Kevrekidis PG, Cuevas-Maraver J, Saxena A, editors. Switzerland AG Cham: Springer Nature; 2020.
- [60] Lederer F, Stegeman GI, Christodoulides DN, Assanto G, Segev M, Silberberg Y. Discrete solitons in optics. Phys Rep 2008;43:1.
- [61] Kartashov YV, Vysloukh VA, Torner L. Soliton shape and mobility control in optical lattices. Prog Opt 2009;52:63.
- [62] Fleischer JW, Segev M, Efremidis NK, Christodoulides DN. Observation of two-dimensional discrete solitons in optically induced nonlinear photonic lattices. Nature 2003;422:147.
- [63] Yang J, Makasyuk I, Kevrekidis PG, Martin H, Malomed BA, Frantzeskakis DJ, Chen ZG. Necklacelike solitons in optically induced photonic lattices. Phys Rev Lett 2005;94:113902.
- [64] Wang XS, Chen ZG, Kevrekidis PG. Observation of discrete solitons and soliton rotation in optically induced periodic ring lattices. Phys Rev Lett 2006;96:083904.
- [65] Kevrekidis PG, Chen ZG, Malomed BA, Frantzeskakis DJ, Weinstein MI. Spontaneous symmetry breaking in photonic lattices theory and experiment. Phys Lett A 2005;340:275.
- [66] Sakaguchi H, Malomed BA. Higher-order vortex solitons, multipoles, and super-vortices on a square optical lattice. Europhys Lett 2007;72:698.

- [67] Chong C, Carretero-González R, Malomed BA, Kevrekidis PG. Multistable solitons in higher-dimensional cubic-quintic nonlinear Schrödinger lattices. *Phys D* 2009;238:126.
- [68] Syafwan M, Susanto H, Cox SM, Malomed BA. Variational approximations for traveling solitons in a discrete nonlinear Schrödinger equation. *J Phys A* 2012;7(45):075207.
- [69] Smerzi A, Trombettoni A. Nonlinear tight-binding approximation for Bose–Einstein condensates in a lattice. *Phys Rev A* 2003;68:023613.
- [70] Carretero-González R, Frantzeskakis DJ, Kevrekidis PG. Nonlinear waves in Bose–Einstein condensates physical relevance and mathematical techniques. *Nonlinearity* 2008;21:R139.
- [71] Kaurov VM, Kuklov AB. Josephson vortex between two atomic Bose–Einstein condensates. *Phys Rev A* 2005;71:011601R.
- [72] Kaurov VM, Kuklov AB. Atomic Josephson vortices. *Phys Rev A* 2006;73:013627.
- [73] Carretero-González R, Talley JD, Chong C, Malomed BA. Multistable solitons in the cubic-quintic discrete nonlinear Schrödinger equation. *Phys D* 2006;216:77–89.
- [74] Susanto H, Hoq QE, Kevrekidis PG. Stability of discrete solitons in the presence of parametric driving. *Phys Rev E* 2006;74:067601.
- [75] Syafwan M, Susanto H, Cox SM. Discrete solitons in electromechanical resonators. *Phys Rev E* 2010;81:026207.
- [76] Syafwan M, Susanto H, Cox SM. Solitons in a parametrically driven damped discrete nonlinear Schrödinger equation. spontaneous symmetry breaking, self-trapping, and Josephson oscillations. In: *Progress optical sci. photonics*; 2013. p. 601.
- [77] Alfimov GL, Korobeinikov AS, Lustrì CJ, Pelinovsky DE. Standing lattice solitons in the discrete NLS equation with saturation. *Nonlinearity* 2019;32(9):3445–3484. 9225
- [78] Muda Y, Akbar FT, Kusdiantara R, Gunara BE, Susanto H. Justification of the discrete nonlinear Schrödinger equation from a parametrically driven damped nonlinear Klein–Gordon equation and numerical comparisons. *Phys Lett A* 2019;383:1274.
- [79] Nicolis G, Prigogine I. *Self-organization in non equilibrium systems*. New York: J Wiley & Sons; 1977.
- [80] Kartashov YV, Torner L, Vysloukh VA. Parametric amplification of soliton steering in optical lattices. *Opt Lett* 2004;29:1102.
- [81] Cai D, Bishop AR, Grønbech-Jensen N. Localized states in discrete nonlinear Schrödinger equations. *Phys Rev Lett* 1994;72:591.
- [82] Hennig D. Periodic, quasiperiodic, and chaotic localized solutions of a driven, damped nonlinear lattice. *Phys Rev E* 1999;59:1637.
- [83] Marin JL, Aubry S. Breathers in nonlinear lattices: numerical calculation from the anticontinuous limit. *Nonlinearity* 1996;9:1501.
- [84] Kivshar YS, Peyrard M. Modulational instabilities in discrete lattices. *Phys Rev A* 1992;46:3198.
- [85] Darmanyan S, Kobayakov A, Lederer F. Stability of strongly localized excitations in discrete media with cubic nonlinearity. *Zh Eksp Teor Fiz* 1998;113:1253. [English translation *J. Exp. Theor. Phys.* 86, 682 1998]
- [86] Iooss G, Joseph DD. *Elementary stability bifurcation theory*. New York: Springer-Verlag; 1980.
- [87] Couillet P. Localized patterns and fronts in nonequilibrium systems. *Int J Bifurc Chaos* 2002;12:2445.
- [88] Clerc MG, Falcon C. Localized patterns and hole solutions in one-dimensional extended systems. *Phys A* 2005;356:48.
- [89] Birnbaum Z, Malomed BA. Families of spatial solitons in a two-channel waveguide with the cubic-quintic nonlinearity. *Phys D* 2008;237:3252.
- [90] Tylutki M, Astrakharchik GE, Malomed BA, Petrov DS. Collective excitations of a one-dimensional quantum droplet. *Phys Rev A* 2020;101:051601(R).
- [91] Press WH, Teukolsky SA, Vetterling WT, Flannery BP. *Numerical recipes in FORTRAN*. Cambridge (UK): Cambridge University Press; 1992.
- [92] Ott E. *Chaos in dynamical systems*. Cambridge, UK: Cambridge University Press; 1993.
- [93] Bland T, Parker NG, Proukakis NP, Malomed BA. Probing quasi-integrability of the Gross–Pitaevskii equation in a harmonic-oscillator potential. *J Phys B* 2018;51:205303.
- [94] Wolf A, Swift JB, Swinney HL, Vastano JA. Determining Lyapunov exponents from a time series. *Phys D* 1985;16:285.
- [95] Eckmann JP, Ruelle D, Ciliberto S. Lyapunov exponents from time series. *Phys Rev A* 1986;34:4971.
- [96] Geist K, Parlitz U, Lauterborn W. Comparison of different methods for computing Lyapunov exponents. *Prog Theor Phys* 1990;83:875.
- [97] Sprott JC. *Chaos and time-series analysis*. UK: Oxford University Press; 2003.
- [98] Scheel JD, Cross MC. Lyapunov exponents for small aspect ratio Rayleigh–Bénard convection. *Phys Rev E* 2006;74:066301.
- [99] Karimi A, Paul MR. Quantifying spatiotemporal chaos in Rayleigh–Bénard convection. *Phys Rev E* 2012;85:046201.
- [100] Gallas JAC. The structure of infinite periodic and chaotic hub cascades in phase diagrams of simple autonomous flows. *Int J Bifurc Chaos* 2010;20:197. And references therein.
- [101] Laroze D, Bragard J, Suarez OJ, Pleiner H. Characterization of the chaotic magnetic particle dynamic. *IEEE Trans Mag* 2011;47:3032; Bragard J, Pleiner H, Suarez OJ, Vargas P, Gallas JAC, Laroze D. Chaotic dynamic of a magnetic nanoparticle. *Phys Rev* 2011;84:037202; Laroze D, Becerra-Alonso D, Gallas JAC, Pleiner H. Magnetization dynamic under a quasiperiodic magnetic field. *IEEE Trans Mag* 2012;48:3567.
- [102] Mahmud MN, Siri Z, Vélez JA, Pérez LM, Laroze D. Chaotic convection in an Oldroyd viscoelastic fluid in saturated porous medium with feedback control. *Chaos* 2020;30:073109; Laroze D, Pleiner H. Thermal convection in a nonlinear non-Newtonian magnetic fluid. *Commun Nonlinear Sci Numer Simul* 2015;26:167; Laroze D, Siddheshwar PG, Pleiner H. Chaotic convection in a ferrofluid. *Commun Nonlinear Sci Numer Simul* 2013;18:2436.
- [103] Clerc MG, Verschuere N. Quasiperiodicity route to spatiotemporal chaos in one-dimensional pattern-forming systems. *Phys Rev E* 2013;88:052916.